# THE EFFECT OF MEMBRANELESS INITIAL CONDITIONS ON THE LATE-TIME DEVELOPMENT OF RICHTMYER-MESHKOV INSTABILITY

**M. M. Mansoor, S. Dalton, T. Desjardins, A. A. Martinez, J. J. Charonko, K. P. Prestridge** †
Physics Division
Los Alamos National Laboratory
Los Alamos, NM 87545, USA
† kpp@lanl.gov

## ABSTRACT

We experimentally investigate the late-time RMI growth of sinuous perturbations of an air/sulfur hexafluoride interface subjected to a Mach 1.2 planar shock wave within the vertical shock tube (VST) facility at Los Alamos National Laboratory. Interface perturbations are established using a novel membraneless technique where cross-flowing Air and $SF_6$ separated by an oscillating splitter plate enter the shock tube to create a perturbed density interface. Late-time mixing widths increase notably for higher $\overline{ka_0}$ initial conditions (where $k$ is the wavenumber and $a_0$ is the initial amplitude) as prescribed by the frequency and sweeping angles of the oscillating plate. We obtain an appropriate scaling to represent our mixing width measurements having a growth exponent $\theta = 0.36$. This compares well with previous membraneless studies (0.3-0.43) which, on average, are found to be $\sim 23\%$ larger than those obtained by membrane experiments.

## INTRODUCTION

The Richtmyer-Meshkov (RM) instability (Richtmyer, 1960; Meshkov, 1970) is the baroclinic generation of vorticity resulting from the misalignment of density and pressure gradients when a density-stratified interface is impulsively accelerated by a shock wave. The instability has drawn significant scientific attention due to its relevance in supernovae explosions and applications in inertial confinement fusion(ICF) in finding a viable fusion-based energy source.

The RM instability can be viewed as a form of Rayleigh-Taylor(RT) instability (Taylor, 1950) in the weak shock limit where the impulsive force is gravitational. Richtmyer (1960) identified the similarities to formulate the linear stability theory for RM flows where the perturbation amplitude grows linearly until becoming comparable to the perturbation wavelength. The linear-amplitude growth rate for a single-mode sinusoidal perturbation between two fluids of different densities ($\rho_1, \rho_2$) is given by:

$$\dot{a} = k \Delta V A^+ a_0^+ \qquad (1)$$

where $a_0$ is the initial amplitude, $k = 2\pi/\lambda$ is the wavenumber, $\Delta V$ is the velocity jump across the interface imparted by the shock and $A = \frac{\rho_2 - \rho_1}{\rho_2 + \rho_1}$ is the Atwood number. The

post-shock values denoted by "$+$" were proposed (Richtmyer, 1960) for having a better agreement between theoretical and computational results. As the amplitude and wavelength become comparable ($ka \approx 1$), nonlinear mechanisms cause perturbations to grow as asymmetrical bubbles and spikes and cause a reduction in growth rate.

The most common method employed in laboratory tests studying the RM instability is to create a perturbed boundary between two gases in a shock-tube. The main hurdle however occurs in forming a well-defined interface between the two gases (Jones & Jacobs, 1997) by methods that do not effect the post-shock flow. Most experiments starting from the earliest work of Meshkov (1969) and his co-workers (Aleshin et al., 1988; Andronov et al., 1995) used a thin sinosoidal nitrocellulose membrane to separate the gases and setup the initial perturbations. While the membrane was shattered by the incident shock wave, the fragment pieces produced are carried with the ensuing flow which affects the late-time development of the RM instability significantly (Jones & Jacob, 1997) for some gas combinations and membrane construction types. More recent studies (Prasad et al., 2000; Jourdan & Houas, 2005) have employed a wire mesh to support the thin nitrocellulose membrane. In this scenario, while the membrane suppresses mixing by isolating the two gases from each other and retarding motions due its inertia and the viscous no-slip condition, the wire mesh enhances mixing by slicing the membrane into ribbons and producing wake-generated turbulence. This can make studying the effect of initial conditions on perturbation growth difficult. The membrane fragments also impede the use of modern visualization techniques such as particle image velocimetry (Prestridge et al., 2000), planar laser-induced florescence (Rightley et al., 1999) and planar Rayleigh scattering (Budzinski et al., 1994).

We develop a novel membraneless method where the undulating motion of a cross-flow is used to set up the initial conditions. An air-foil flapper, upstream from the test section is used to oscillate the cross-flow at various frequencies and amplitudes. The technique allows us to produce sinuous perturbations for $\overline{ka_0} = 0.30 - 0.86$ so that we can determine the effect of systematically increasing $\overline{ka_0}$ values on the late-time development of the RM instability. For the experimental conditions employed ($Ma = 1.2, At \sim 0.67$), the results are used to obtain a dimensional scaling for perturbation growth and compared with previous membrane and
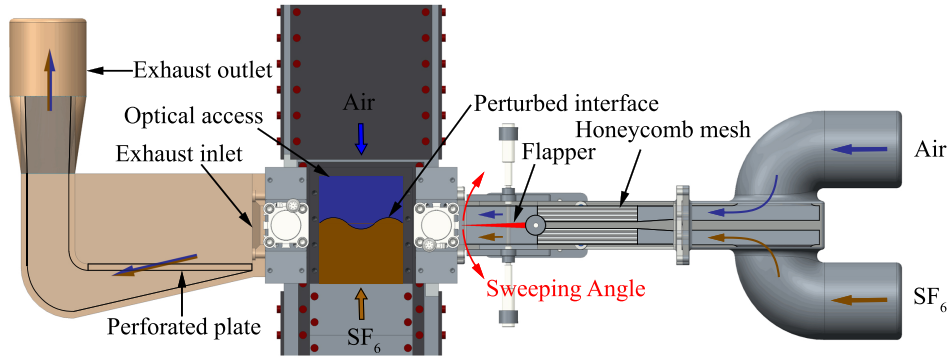
Figure 1.    Closeup overview of the initial condition interface setup at station 1.

membraneless studies.

## EXPERIMENTAL SETUP

All experiments are conducted at the Los Alamos National Laboratory (LANL) Vertical Shock Tube (VST) facility. A diaphragmless plug and sleeve two-piston driver (Mejia-Alvarez *et al.*, 2015) is used to produce a Mach 1.2 planar shock wave in a 7 m tall $127 \times 127$ mm square cross-section shock-tube. The VST consists of three diagnostic stations. A close-up of station 1 is given in Fig. 1 while Station 2 & 3 are situated $x = 28$ cm and 63 cm downstream. Air is filled from the top and $SF_6$ from the bottom until the two gases meet and start exiting through the outlet (on the left) at station 1. This creates a stagnation point flow at the interfacial location that has the added effect of thinning the diffusion layer. The air (upper side inlet) and $SF_6$ (lower side inlet) cross-flow is first streamlined individually by passing through a two-part honeycomb mesh. Flapper oscillations at the mesh exit then produces an undulating cross co-flow that enters the test-section at 0.2 m/s through a $12.70 \times 3.81$ cm channel to form a perturbed interface. The cross-flow is vented out from the exhaust opposite to the inflow to prevent any accumulation within the shock-tube from causing unwanted disruptions to the interface. The steady-state flapper oscillation frequency and total rotation angle used ranged between 0.25-3 Hz and $8 - 16°$.

When the driver is depressurized to generate a shock wave, two pneumatically driven gates close the inlet and outlet at each end of the test-section (see Fig. 1). This prevents effects from side-wall openings that can weaken the incident shock-wave, introduce non-uniformities and also damage the flapper mechanism. The shock location is monitored using six pressure transducers as it travels down the tube from the driver. The pressure signals are also used to trigger the optical diagnostic systems at each station. All operations including timing, servo-motors, test-section gates, flapper, shock driver, gas flows and diagnostics are controlled using LabVIEW.

2-D particle image velocimetry (PIV) diagnostics image the initial conditions and ensuing structures. Six single-pulse Nd:YAG lasers operating at 532nm wavelength are used for PIV measurements, and the flow is seeded with olive oil particles (mixed with $SF_6$ bulk and cross-flow using a Laskin-nozzle). An optical train (spherical lens followed by cylindrical lens) is used to shape the laser beam into a thin diverging light sheet and directed into the the shock-tube longitudinally, using a 45° angled mirror at the bottom at station 1 and laterally from sides at stations 2 &

3. The flow fields are visualized at each station using a TSI PowerView camera having a $4008 \times 2672$ charged couple device (CCD) array. A single image is taken at station 1 just prior to the arrival of the shock wave ($t = 0$ ms) while a pair (7 $\mu$s interframe delay) is recorded at station 2 and 3. The image pairs are processed using a 3-pass recursive cross-correlation algorithm with a final window size of $32 \times 32$ pixels at 50% overlap which translated to a 464 $\mu$m vector spacing.

### Interface characterization

Characterizing the interface for each flapper condition is crucial given the objective of this study to determine the effect of initial conditions on the late-time development of the RM instability. Three different sets of initial conditions are investigated using a combination of oscillating plate frequencies, $f$(Hz), and sweeping angles, $\triangleleft(°)$, (see Table 1). Figure 2(top row) shows initial interface images for (*a*) 0.25 Hz, 8°, (*b*) 3 Hz, 8° and (*c*) 3 Hz, 16°. As observed, despite the automation schemes considered to initialize the perturbations, the interface is not found to be perfectly sinusoidal. This is particularly noticeable for larger flapper frequencies and sweeping angles where the asymmetric and multi-modal features are more pronounced but a dominant wavelength and amplitude are still noticeable. We obtain initial amplitudes and wavelengths by finding average values for each experiment (Jacobs *et al.*, 2013) which are then ensemble-averaged over all realizations ($\overline{a_0}$, $\overline{\lambda_0}$) for each flapper condition investigated with the corresponding variations(standard deviations) listed in Table 1.

Table 1.   Flapper oscillation parameters and corresponding initial interface characteristics.

| $f$(Hz) | $\triangleleft(°)$ | $\overline{\lambda_0}$(mm) | $\overline{a_0}$(mm) | $\overline{ka_0}$ |
|---------|-----|------------|------------|--------|
| 0.25 | 8 | $29.1 \pm 3.7$ | $1.37 \pm 0.17$ | 0.30 |
| 3 | 8 | $19.7 \pm 1.8$ | $1.65 \pm 0.18$ | 0.53 |
| 3 | 16 | $18.3 \pm 1.1$ | $2.51 \pm 0.15$ | 0.86 |
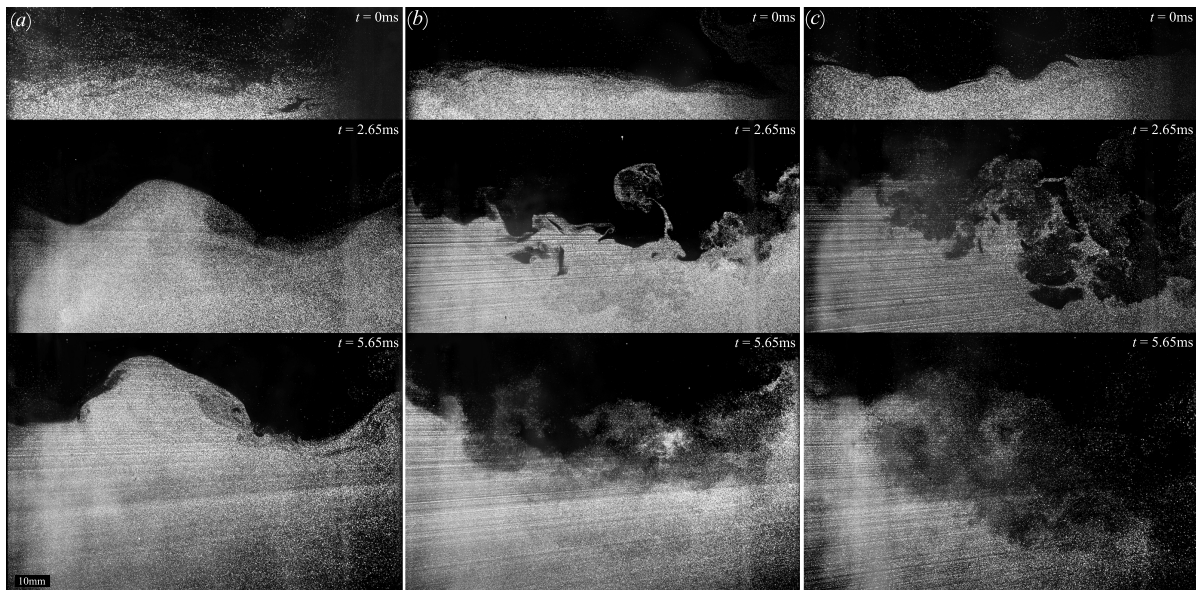
Figure 2. Particle image velocimetry images at $t = 0, 2.65, 5.65$ ms for $\overline{ka_0} = $ (a) 0.3, (b) 0.53 and (c) 0.86.
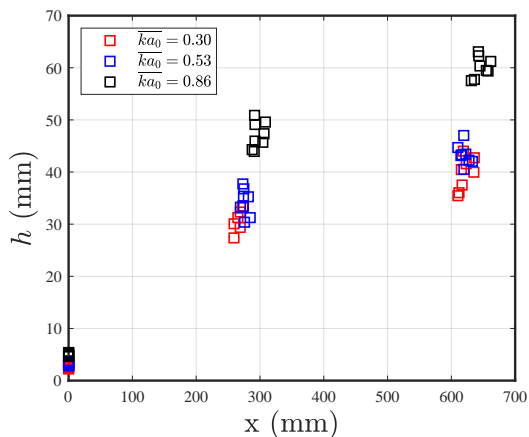


Figure 3. Effect of initial conditions on mixing widths with respect to downstream distance. Mean values at $x \approx 280$ mm are $h$(mm) $= 31.3, 34.2, 47.1$ and at $x \approx 630$ mm are $h$(mm) $= 39.7, 43.3, 60.1$ for ($\square$, $\square$, $\square$), respectively.

## RESULTS

The evolution of the RM instability for increasing $ka_0$ initial conditions is shown in Fig. 2. The first image shows the interface just prior to the arrival of the shock wave ($t =0$ ms) while the second and third are recorded at $t = 2.65$ and $5.65$ ms, respectively. The differences are dramatic where the baroclinic vorticity roll-up into bubbles of air separating spikes of $SF_6$ disintegrate into diffuse structures notably earlier for larger $ka_0$. While the dominant-wavelength with some small length-scales are preserved at the lowest $\overline{ka_0}$, mixing and transition to smaller scales is noted evidently for $\overline{ka_0} = 0.53$ and $0.86$ as early as $t = 5.65$ and $2.65$ ms, respectively. Secondary RM instabilities (Peng *et al.*, 2003) following the primary baroclinic vorticity deposition (occurring from the misalignment of pressure gradient across the shock wave and density gradient across the interface) have been shown to greatly enhance mixing which eventually triggers a transition to turbulence. This secondary vorticity deposition dominates at intermediate times due to the misalignment of density gradient across the interface and vortex-centripetal acceleration arising from the large-scale rotation of coherent vortices formed by the primary vorticity roll-up. More explicitly, opposite-sign vorticities generated at the neck and arms of the mushroom structures are advected into the vortex core. This local fluid entrainment causes mixing and the structure to disintegrate accordingly.

A spectrum of unwanted small-amplitude short-wavelength perturbations (Vandenboomgaerde *et al.*, 2014) due to experimental imperfections and presence of multi-mode fronts can cause vortex pairing and mode coupling (Yang & Zabuski, 1989) in the nonlinear late-time growth regime. Large scales develop by means of a bubble-competition mechanism (Zufria, 1988) and vortex pairing when multiple dominant wavelengths are present (Rupert, 1991). As each bubble tries to occupy the maximum possible space and compete with others, smaller bubbles advance less due to lower speeds (Layzer, 1955). This causes them to shrink and slow down while larger ones expand and acquire higher vortex speeds. Eventually, bubbles overtake their smaller neighbors to form a larger bubble, also known as a "bubble merger" (Sharp, 1984; Glimm *et al.*, 1990). This imbalance in cross-coupling strengths may also induce a tilt effect on the interface. For example, a clockwise interface tilt at late-times ($t =2.65$, $5.65$ ms) is noted for the highest $\overline{ka_0}$ in Figure 2(c) where a right-sided descent occurs towards small amplitude perturbations. This disturbs the evolution of some adjacent bubbles and spikes further from growing into each other. A similar tilting feature and disruption in mushroom structures was also noted in gas-curtain experiments (Orlicz *et al.*, 2013) from disparities in counter-rotating vortex strengths.

The perturbations break-up at late-times to form mixing regions which then makes it difficult to determine the shape of the interface. We define the mixing layer width $h$ as the distance between spike and bubble tips with a mean amplitude, $a = h/2$. The images are first corrected for non-uniform illumination using morphological opening and adjusted background subtraction. Spanwise-averaging is then performed to obtain a mean olive oil concentration distribution and the mixing width is measured as the streamwise distance between 5% and 95% values of the average con-
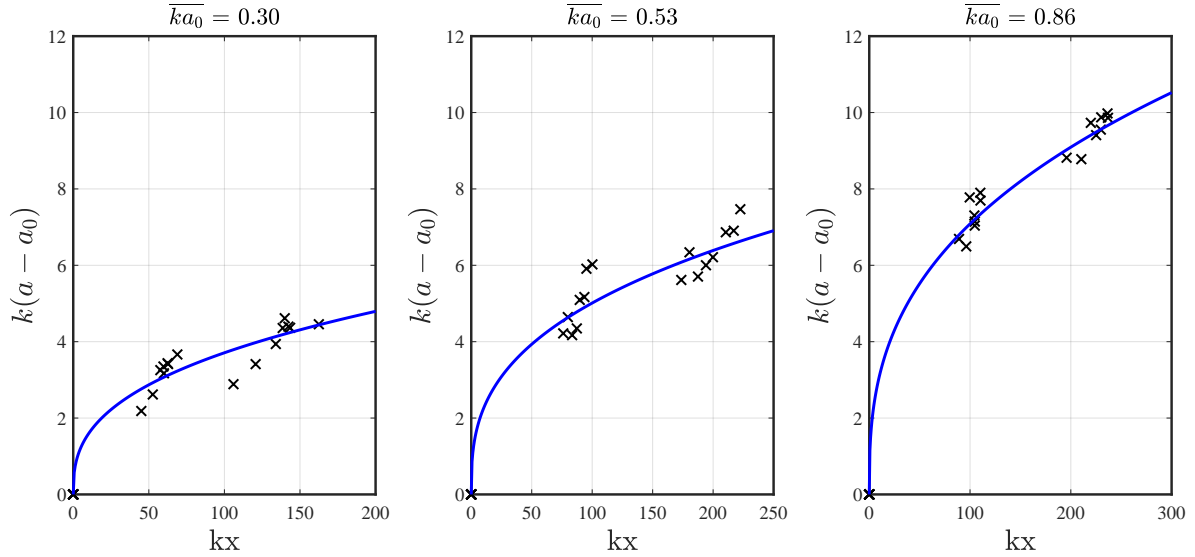
Figure 4. Dimensionless amplitude as a function of normalized distance for $\overline{ka_0} = 0.3$, 0.53 and 0.87(See Table 1 for details). Power law fits follow $k(a - a_0) \propto (kx)^n$ where $n = 0.37, 0.35, 0.36$, respectively.
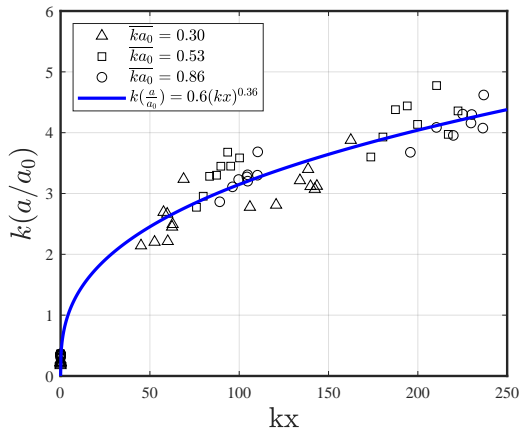


Figure 5. Dimensional-scaling $k(\frac{a}{a_0}) = 0.6(kx)^{0.36}$ collapses the data for $\overline{ka_0} = 0.30 - 0.86$.

centration profile.

Growth in mixing widths with downstream distance are shown in Figure 3. As observed, higher $\overline{ka_0}$ initial conditions result in larger growths with the increase being notably significant for the highest $\overline{ka_0}$. Normalizing the data with respect to wavenumber $k$ highlights this effect further in terms of non-dimensional amplitude. Power-law exponents from fits to the data are found to range between 0.35-0.37 for $\overline{ka_0} = 0.30 - 0.86$. Finding an empirical relation which generalizes the growth of all initial conditions herein, the dimensional scaling

$$k\left(\frac{a}{a_0}\right) = 0.6(kx)^{0.36} \qquad (2)$$

is able to provide an appropriate fit where all lengths are in mm.

The late-time growth of the mixing zone has been suggested by a number of researchers (Mikaelian, 1989; Alon et al., 1995; Zhou, 2017) to follow a power-law behavior $h \sim t^\theta$ where the determination of the scaling exponent $0.2 \lesssim \theta \lesssim 0.6$ has been a subject of active research. Our generalized scaling exponent (0.36) is found to be in good agreement with those by Jacobs et al., (2013) (0.3-0.4) and close to Weber et al., (2014) ($0.43 \pm 0.01$), both of which used membraneless techniques to impose the initial conditions. Values by Krivets et al., (2017) varied over a large range (0.19-0.57) having ensemble averages of $\theta_b = 0.38$ and $\theta_s = 0.4$ for bubble and spike growth exponents, respectively. Laser-driven experiments by Dimonte & Schneider (1997) found $\theta = 0.5 \pm 0.1$ for $At \sim 0.9$. Later Dimonte & Schneider (2000) found bubbles and spike responses of $\theta_b = 0.25$ and $\theta_s = 0.3$ (for $A \sim 0.7$). However, to compensate for demixing caused by any residual deceleration in their linear electric motor system (Dimonte et al., 1996), it was suggested that these exponents may have to be increased by $\sim 10\%$. Experiments performed using membranes by Prasad et al., (2000) in comparison produced a late-time growth exponent of ($0.26 \leq \theta \leq 0.33$). Although more experiments are needed to ascertain the influence of membranes on the growth rate accurately, comparing our results with studies employing shock-tube set-ups for similar shock strengths and Atwood numbers (Prasad et al., (2000); Jacobs et al., 2013; Weber et al., 2014; Krivets et al., 2017) indicates membrane remnants suppress the growth exponent $\theta$ on average by $\sim 23\%$. This is similar to the 20% amplitude reduction obtained by Mariani et al., (2008) in the non-linear stage in comparison with theoretical models.

## CONCLUDING REMARKS

We perform an experimental investigation to determine the effect of initial conditions on the late-time growth of Richtmeyer-Meshkov(RM) instability. A flapper-based mechanism consisting of an oscillating airfoil is used to induce perturbations on an air-$SF_6$ interface with $\overline{ka_0} = 0.30 - 0.86$. Larger mixing widths are obtained for higher $\overline{ka_0}$ initial conditions. A combination of interfacial parameters is used to obtain $k\left(\frac{a}{a_0}\right) = 0.6(kx)^{0.36}$ as an appropriate scaling for $A \sim 0.67$ and Mach 1.2 where the scaling

factor (0.36) is found to be in close agreement with previous membraneless studies (0.3-0.43, Weber *et al.*, 2014; Jacobs *et al.*, 2013). A comparison with past membrane experiments (Prasad *et al.*, 2000) for similar Atwood numbers and shock strengths reveals an average growth exponent reduction of $\sim 23\%$. It is noteworthy that the flapper-based interface and those produced by past membraneless studies discussed herein are diffuse which tend to have a reducing effect on the RM instability growth rate (Jones & Jacob, 1997; Collin & Jacob, 2002; Morgan *et al.*, 2016). The suppression in growth exponent caused by the use of membrane hence could be even larger in comparison to studies employing a discontinuous interface configuration with no supports (Liu *et al.*, 2018).

## REFERENCES

Aleshin, A. N., Gamalii, E. G., Zaitsev, S. G., Lazareva, E. V., Lebo, I. G., Rozanov, V. B., 1988 Nonlinear and transitional states in the onset of the Richtmyer-Meshkov instability. *Sov. Tech. Phys. Lett.* **14**, 466.

Alon, U., Hecht, J., Ofer, D. & Shvarts, D. 1995 Power laws and similarity of Rayleigh-Taylor and Richtmyer-Meshkov mixing fronts at all density ratios. *Phys. Rev. Lett.* **74** (4), 534–537.

Andronov, V. A., Zhidov, I. G. & Meskov, E.E. 1995 Computational and experimental studies of hydrodynamics instabilities and turbulent mixing. *Los Alamos National Lab.*, NM (USA) pp. 1–108.

Budzinski, John M., Benjamin, Robert F. & Jacobs, Jeffrey W. 1994 Influence of initial conditions on the flow patterns of a shock-accelerated thin fluid layer. *Phys. Fluids* **6** (11), 3510–3512.

Collins, B. D. & Jacobs, J.W. 2002 PLIF flow visualization and measurements of the Richtmyer-Meshkov instability of an air/SF6 interface. *J. Fluid Mech.* **464**, 113–136.

Dimonte, G., Morrison, J., Hulsey, S., Nelson, D., Weaver, S., Susoeff, A., Hawke, R., Schneider, M., Batteaux, J., Lee, Dean, L. & Ticehurst, J. 1996 A linear electric motor to study turbulent hydrodynamics. *Rev. Sci. Instrum.* **67**(1), 302–306.

Dimonte, G. & Schneider, M. 2000 Density ratio dependence of Rayleigh-Taylor mixing for sustained and impulsive acceleration histories. *Phys. Fluids* **12**(2), 304–321.

Glimm, J., Li, X. L., Menikoff, R., Sharp, D. H. & Zhang, Q. 1990 A numerical study of bubble interactions in Rayleigh-Taylor instability for compressible fluids. *Phys. Fluids A* **2**(11), 2046–2054.

Jacobs, J. W., Krivets, V. V., Tsiklashvili, V. & Likhachev, O. A. 2013 Experiments on the Richtmyer-Meshkov instability with an imposed, random initial perturbation. *Shock Waves* **23**(4), 407–413.

Jones, M. A. & Jacobs, J. W. 1997 A membraneless experiment for the study of Richtmyer-Meshkov instability of a shock-accelerated gas interface. *Phys. Fluids* **9**(10), 3078–3085.

Jourdan, Georges & Houas, Lazhar 2005 High-amplitude single-mode perturbation evolution at the Richtmyer-Meshkov instability. *Phys. Rev. Lett.* **95**(20), 1–4.

Krivets, V. V., Ferguson, K. J. & Jacobs, J. W. 2017 Turbulent mixing induced by Richtmyer-Meshkov instability. *AIP Conference Proceedings* **1793**, 150003.

Layzer, D. 2002 On the Instability of Superposed Fluids in a Gravitational Field. *Astrophys. J.* **122**(604), 1–12.

Liu, L., Liang, Y., Ding, J., Liu, N. & Luo, X. 2018 An elaborate experiment on the single-mode Richtmyer-Meshkov instability. *J. Fluid Mech.* **853**, R2.

Mariani, C., Vandenboomgaerde, M., Jourdan, G., Souffland, D. & Houas, L. 2008 Investigation of the Richtmyer-Meshkov instability with stereolithographed interfaces. *Phys. Rev. Lett.* **100**(25), 1–4.

Mejia-Alvarez, R., Wilson, B., Leftwich, M. C., Martinez, A. A. & Prestridge, K. P. 2015 Design of a fast diaphragmless shock tube driver. *Shock Waves* **25**(6), 635–650.

Meshkov, E. E. 1969 Instability of the interface of two gases accelerated by a shock wave. *Fluid Dyn.* **4**(5), 101–104.

Mikaelian, K. O. 1989 Turbulent mixing generated by Rayleigh-Taylor and Richtmyer-Meshkov instabilities. *Physica D: Nonlinear Phenomena* 36, 343–357.

Morgan, R. V., Likhachev, O. A. & Jacobs, J. W. 2016 Rarefaction-driven Rayleigh–Taylor instability. Part 1. Diffuse-interface linear stability measurements and theory. *J. Fluid Mech.* **791**, 34–60.

Orlicz, G. C., Balasubramanian, S. & Prestridge, K. P. 2013 Incident shock Mach number effects on Richtmyer-Meshkov mixing in a heavy gas layer. *Phys. Fluids* **25**(11), 1–28.

Prasad, J. K., Rasheed, A., Kumar, S. & Sturtevant, B. 2000 The late-time development of the Richtmyer-Meshkov instability. *Phys. Fluids* **12**(8), 2108–2115.

Prestridge, K. P., Vorobieff, P., Rightley, P. M. & Benjamin, R. F. 2000 Validation of an instability growth model using particle image velocimetry measurements. *Phys. Rev. Lett.* **84**(19), 4353–4356.

Richtmyer, R. D. 1960 Taylor instability in shock acceleration of compressible fluids. *Comm. Pure Appl. Math.* **13**(2), 297–319.

Rightley, P. M., Vorobieff, P., Martin, R. & Benjamin, R. F. 1999 Experimental observations of the mixing transition in a shock-accelerated gas curtain. *Phys. Fluids* **11**(1), 186–200.

Rupert, V. 1992 Shock-interface interaction: Current research on the Richtmyer-Meshkov problem. *K. Takayama (ed.), Shock Waves* pp. 1–14.

Sharp, D. H. 1984 An overview of Rayleigh-Taylor instability. *Los Alamos National Lab.*, NM (USA) pp. 3–18.

Taylor, G. I. 1950 The instability of liquid surfaces when accelerated in a direction perpendicular to their planes. I. *Proc. R. Soc. Lond. A Math. Phys. Sci.* **202**(1068), 81–96.

Vandenboomgaerde, M., Souffland, D., Mariani, C., Biamino, L., Jourdan, G. & Houas, L. 2014 An experimental and numerical investigation of the dependency on the initial conditions of the Richtmyer-Meshkov instability. *Phys. Fluids* **26** (2).

Weber, C. R., Haehn, N. S., Oakley, J. G., Rothamer, D. A. & Bonazza, R. 2014 An experimental investigation of the turbulent mixing transition in the Richtmyer-Meshkov instability. *J. Fluid Mech.* **748**, 457–487.

Yang, X. & Zabuski, N. J. (1989) Shock induced dipolar vortex structure and comoressible turbulence. In: Rupert V (cd) Proc. Internat. Exchange on RM and RT Mixing.

Zhou, Y. 2017 Rayleigh–Taylor and Richtmyer–Meshkov instability induced flow, turbulence, and mixing. I. *Phys. Repts* **720-722**, 1–136.

Zufiria, J. A. 1988 Bubble competition in Rayleigh–Taylor instability. *Phys. Fluids* **31**(3), 440-446.